International Journal of Thermophysics (2023) 44:167
https://doi.org/10.1007/s10765-023-03283-2

Thermal Conductivity of Gas Diffusion Layers of PEM Fuel Cells: Anisotropy and Effects of Structures

Qusai Alahmad[1] · **Mahya Rahbar**[1] · **Meng Han**[2] · **Huan Lin**[3] · **Shen Xu**[4] · **Xinwei Wang**[1]

Received: 13 October 2023 / Accepted: 20 October 2023

Abstract

When addressing the proton exchange membrane (PEM) fuel cells, effective water management is essential for the system to respond promptly to electric power demands. The local water vapor saturation pressure and interphase mass transfer are impacted by the temperature distribution inside the structure whereas the gas diffusion layer (GDL) is crucial in facilitating effective heat transfer during cell operation. This work is focused on obtaining a better understanding of the thermal conductivity (k) of the gas diffusion layer in two arrangements, single uncoated macro-porous layer GDL without polytetrafluoroethylene (PTFE), and as a coated double-layer consisting of GDL with 50 % PTFE and a micro-porous layer (MPL). The k in the in-plane and out-of-plane directions of the double-layer GDL improved by 50 % and 184 % in vacuum, respectively, compared with the case where it is uncoated and unsupported by MPL. Also, this study represents one of the first to investigate the k of double-layer GDL in the in-plane direction. Our out-of-plane k measurement in air and vacuum provides deep insight into the heat transfer mechanism of the porous GDL: the sample and pores inside it follow more parallel configurations than serial for the uncoated macro-porous layer sample, while quite serial configurations for the double-layer GDL sample.

Keywords Gas diffusion layer · In-plane thermal conductivity · Out-of-plane thermal conductivity · Structural effect

1 Introduction

The gas diffusion layer (GDL) plays a vital role in the diffusion of reactant gases and the management of water in proton exchange membrane (PEM) fuel cells [1–4]. PEM fuel cells were presented as a viable power source for automotive and

---

Qusai Alahmad and Mahya Rahbar are equal contribution authors.

Extended author information available on the last page of the article stationary applications due to their capability of producing high power densities, even when subjected to rapid load changes [5, 6]. But, for the system to respond promptly to electric power demands, effective water management is essential [1, 2]. Reduced ionic conductivity between the membrane and catalyst layer (CL), as well as the creation of considerable resistance between the membrane and the CL, are caused by insufficient water levels. Conversely, too much water in the membrane-electrode assembly (MEA) reduces the number of active sites accessible for electrochemical reactions and prevents the transport of reactants across non-reactive regions. At the cathode CL, liquid water is created when water vapor condenses, and an oxygen reduction process occurs. This liquid water then migrates into the membrane or the GDL [1, 2]. This GDL can be either a single or a double-layer.

Single-layer GDL, usually a carbon-based material product, could be woven carbon cloth, non-woven carbon paper, carbon felt, and carbon foam [1, 7]. This single-layer arrangement will be referred to here as the macro-porous layer. Due to its high porosity, carbon fiber-based paper has traditionally provided effective pathways for gas and water to move through the fuel cell. Before adding the macro-porous layer to the cell assembly, it must be wet-sealed with polytetrafluoroethylene (PTFE) coatings [8]. This wet-sealing is to avoid clogging the pores with water. Moreover, this helps regulate the quantity of water carried to and retained at the cell membrane for hydration to aid in water management [7, 9]. Wet-proofing the layer with such a hydrophobic coating also increases the pores in the GDL, which eases gas transport to the catalyst cathode or anode layer [2, 4, 7].

On the other hand, double-layer GDL consists of two layers, first the same macro-porous carbon layer constructing the single GDL, supported by a second layer, which is a micro-porous layer (MPL) made out of carbon black mixed with PTFE [7]. MPL is mainly used as a support to the single-layer GDL, which helps mitigate limitations that the single-layer GDL has, like limited electrical contact resistance with the catalyst layer. MPL here acts as a flat, homogeneous layer impermeable to the catalyst particles. Furthermore, it improves water management and electrical conductivity in the membrane electrode assembly, which increases fuel cell efficiency [1, 4, 10].

During cell operation, GDL is also essential for facilitating efficient heat transfer, as the temperature distribution inside the structure affects the local water vapor saturation pressure and interphase mass transfer. The thermal conductivity of the GDL is closely related to its water transport characteristics [11]. Herein, a double-layer GDL (50 % PTFE + MPL) and an uncoated single-layer GDL (0 % PTFE) are studied to show that the thermal conductivity of GDL is very different in the in-plane direction from that in the out-of-plane direction, which is explained by detailed anisotropic structure. The macro-porous layer is studied here twice for contrast, first as an individual uncoated (0 % PTFE) test subject, then as a coated part of the whole double-layer GDL. The single-layer GDL studied here consists of only the macro-porous layer. We will directly compare all single-layer GDLs in some aspects before and after coating. The double-layer GDL layers are inseparable, so the coated macro-porous layer is studied as a part of the entire double-layer GDL.

The thermal conductivity of GDLs was studied in many previous studies [12–17] in different directions, out-of-plane or in-plane, under different conditions of temperature and pressure, whether it is uncoated with PTFE or coated with different ratios, supported by an MPL, or unsupported. For example, Khandelwal and Mench's study in the out-of-plane direction [12] on SIGRACET series AA carbon paper (0 % PTFE) at 56 °C would serve as a direct comparison for our uncoated macro-porous layer's (0 % PTFE) thermal conductivity in the out-of-plane direction. In addition, Karimi et al.'s [13] study on the out-of-plane thermal conductivity of SolviCore DGL (30 % PTFE + MPL) at 70 °C under different pressures would serve as a comparison with our double-layer GDL (50 % PTFE + MPL) in the out-of-plane direction. Moreover, the study in the in-plane direction by Zamel et al. [18] on TORAY-TPGH-120 (0 % PTFE), which is not supported by MPL and has no PTFE treatment, could serve as a direct comparison for our uncoated macro-porous layer (0 % PTFE) thermal conductivity in the in-plane direction. However, it appears that none of the studies investigated the thermal conductivity of the double-layer GDL (50 % PTFE + MPL) in the in-plane direction. Therefore, this study will be one of the first studies in the field to do so.

Moreover, few to none of those aforementioned studies addressed the thermal conductivity anisotropy of GDL. At the same time, this characteristic is critical to understanding the GDL structure and heat conduction capacity. This study aims to investigate the intrinsic thermal conductivity of the single- and double-layer GDL and shows that the GDLs have highly anisotropic thermal conductivities. Two techniques will be used to measure the thermal conductivity: the transient electro-thermal (TET) [19] technique for the in-plane thermal conductivity measurement and the differential thermal resistance (DTR) technique [20] for the out-of-plane thermal conductivity measurement. Our lab introduced, calibrated, and validated both techniques for a wide variety of materials. Additionally, the out-of-plane thermal conductivity is measured in vacuum and air conditions to study the effect of pores on thermal conductivity, which is a critical feature of GDL layers.

2 Materials and Methods

2.1 Material Structure

Samples of both double-layer GDL (50 % PTFE + MPL) and uncoated macro-porous layer (0 % PTFE, carbon paper) are products of Suzhou Sinero Technology Co., Ltd, where the double-layer GDL product number is YSL-20, and uncoated macro-porous layer (in form of a carbon paper), has a product number of HCP010N. Double-layer GDL studied here consists of two layers, shown in Fig. 1a. The first of these two layers is a macro-porous carbon layer, also known as a single-layer GDL, that could be non-woven carbon paper or a woven texture [7]. Figure 1b shows the structure inside the cell. As can be seen, the MPL supports the macro-porous layer and sits between that layer and the CL, where it acts as a flat, homogeneous layer impermeable to the catalyst particles. Furthermore, it improves water management in the membrane electrode assembly, which increases fuel cell efficiency [1, 10]. For comparison purposes, the single-layer GDL is studied here as an individual uncoated test subject and as a coated

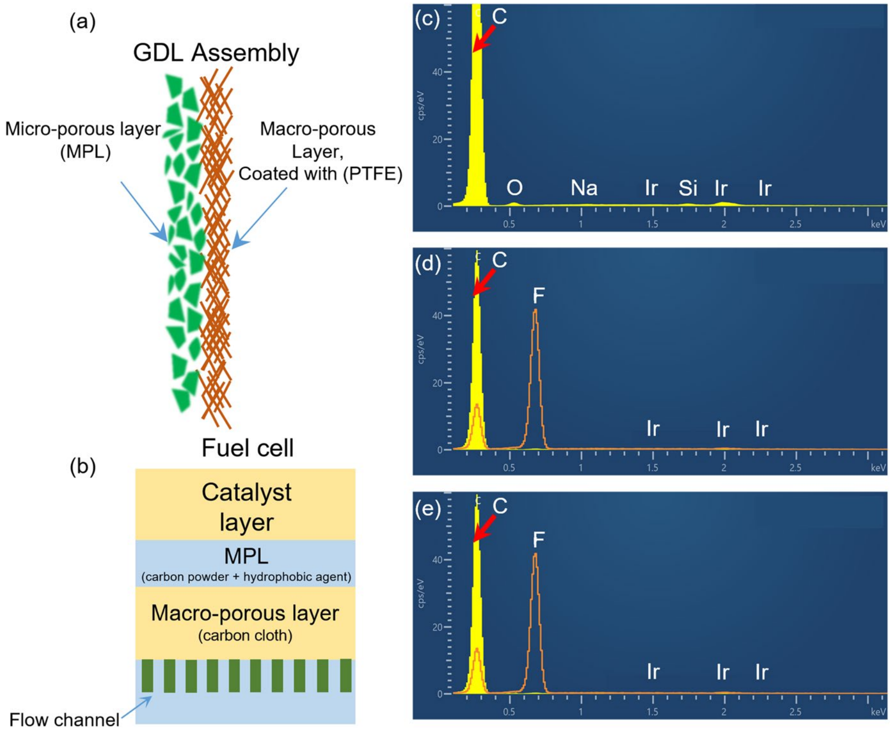

Fig. 1 (a) Detailed arrangement of the double-layer GDL assembly with the macro-porous layer (right) and the MPL (left). (b) The structure inside the fuel cell, the MPL, supports the macro-porous layer and is between it and the CL. (c) The EDS results of the uncoated macro-porous layer. (d) The EDS results of the coated macro-porous layer. (e) The EDS results of the MPL

part of the entire GDL assembly. The double-layers GDL layers are inseparable; therefore, the coated macro-porous layer is studied as a part of the whole double-layer GDL. Both macro-porous carbon layers studied here are made out of fragile non-woven carbon fibers. This layer, before adding it to the cell assembly, needs to be wet sealed with a PTFE coating [8] to avoid pore clogging with water. Moreover, this help regulates the quantity of water carried to and retained at the cell membrane for hydration to aid in water management [7, 9]. Wet-proofing the layer with such a hydrophobic coating also increases the pores in the GDL, which eases gas transport to the catalyst cathode or anode layer [7]. Figure 1c, d shows the energy-dispersive x-ray spectroscopy (EDS) results of both the uncoated and coated macro-porous layer samples, respectively. The uncoated sample is pure carbon (0 % PTFE), while in the coated one, the fluorine percentage reaches ~ 50 % in some spots, suggesting an uneven coating texture.

The second layer constructing the double-layer GDL is an MPL consisting of carbon black mixed with PTFE [7]. The MPL is mainly used as a support to the single-layer GDL. It helps mitigate limitations that the single-layer GDL has, like limiting the electrical contact resistance with the catalyst layer [10]. Figure 1e shows the EDS results of MPL. Similar to the coated macro-porous layer, the fluorine percentage could reach ~ 50 % in some spots, suggesting an uneven coating texture.

2.2 Material Properties

Figure 2a, top depicts the scanning electron microscopy (SEM) image of the macro-porous layer before and after being coated. The pores are clear to see with the naked eye. The uncoated layer thickness and density were measured to be 0.1 mm and 0.39 g · cm^{-3}, respectively. Similarly, the MPL structure can be seen in the SEM images in Fig. 2a, top. The structure is more rigid than the macro-porous layer. The double-layer GDL's thickness is measured to be 0.2 mm, while the density is 0.79 g · cm^{-3}.

Figure 2b shows the Raman spectra for the three samples, including both faces of the double-layer GDL (the coated macro-porous face and the MPL face), and the uncoated macro-porous layer. The spectra are taken at two selected spots for

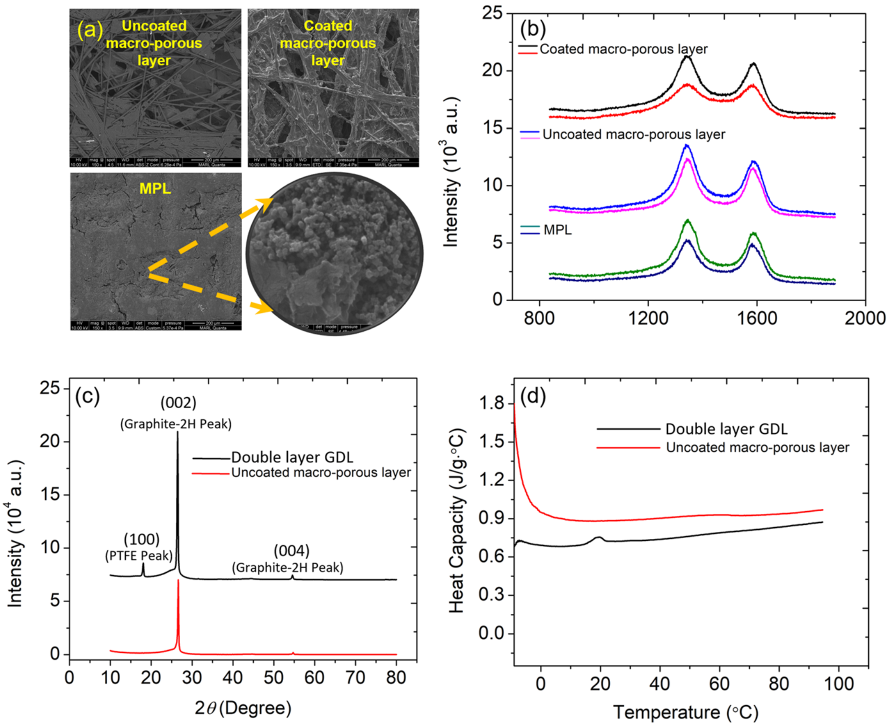

Fig. 2 (a) The top depicts the scanning electron microscopy image (SEM) of the macro-porous layer before and after being coated. The bottom are the SEM images of MPL, whose structure is more rigid than the macro-porous layer. (b) Raman spectra for the coated macro-porous layer, uncoated macro-porous layer, and MPL. (c) XRD patterns of the uncoated macro-porous layer and the double-layer GDL. (d) DSC measurement of the specific heat for the uncoated macro-porous layer, and the double-layer GDL, from 0 to 100 °C

each sample. As can be seen, the uncoated macro-porous layer shows stronger and sharper peaks between 1200 cm^{-1} and 1600 cm^{-1}. These peaks are the D-band and the G-band from left to right, respectively. The D-peak at (1344 cm^{-1}) indicates that the sample has defects and is not a single crystal [21].

In Fig. 2c where the XRD results are shown, the (002) plane peak is very sharp, which tells that the material structure is very close to graphite and very crystalline. Nevertheless, the wide Raman peaks suggest the material around the edges is a bit disordered or that the material is carrying some impurities. As a pure carbon sheet, the uncoated macro-porous layer has two peaks for the planes (002) and (004). While the double-layer GDL has three peaks, in addition to the peaks of the (002) and (004) planes, it also has a peak from PTFE for the (100) plane. To calculate the size of the crystallite, the Scherrer equation is used [22]:

$$\tau = \frac{K\lambda}{\beta \cos\theta}, \tag{1}$$

where τ is the crystallite size, K shape factor, λ x-ray wavelength, β full width at half maximum of peaks (FWHM) in radian located at any 2θ, and θ the Bragg angle. Solving Eq. 1 and taking the peaks in the three planes (002), (004), and (100), their d-spacing is determined to be 3.38 Å, 1.68 Å, and 4.91 Å, respectively. The (002) peak, associated with 3.38 Å d-spacing in the uncoated macro-porous layer, and when compared with Sun et al.'s [23] study and their XRD analysis on natural graphite, where they found that the d-spacing at (002) peak is 3.40 Å, suggests that our sample pretty much reserves the crystallite structure of graphite. The crystallite sizes are determined to be 26.9 nm, 25.3 nm, and 20.4 nm in the (002), (004), and (100) directions, respectively, indicating our carbon sample has quite sphere-like crystalline grains. Please note that K and λ are taken as 0.89 and 1.5432 Å, respectively. Additionally, for the uncoated macro-porous layer, the degree of crystallinity is estimated by integrating the area under the peaks (the crystalline part of the sample) and then comparing it with the total area of the diffractogram. For our sample, the crystallinity is determined to be 87.4 %, which leads to the conclusion that the wide Raman peaks are most likely associated with the material carrying some impurities.

Figure 2d illustrates the heat capacity (c_p) results based on differential scanning calorimetry (DSC) done on both the uncoated macro-porous layer and the double-layer GDL. The temperature ranges from 0 °C up to 100 °C. Similar behavior can be observed after 0 °C, where the c_p value has a gradual growth for both samples towards 100 °C. The heat capacity around the room temperature is found to be 882 $J \cdot kg^{-1} \cdot K^{-1}$ for the uncoated macro-porous layer and 732 $J \cdot kg^{-1} \cdot K^{-1}$ for the double-layer GDL. The value of c_p for graphite was found previously as 709 $J \cdot kg^{-1} \cdot K^{-1}$ [24]. Our sample's c_p is higher than that of pure graphite, possibly due to the PTFE coating and impurities in the carbon structure. Please note that, a TA Discovery DSC 2500 machine is used to determine the c_p. Hence, the c_p uncertainty is a function of the temperature accuracy, the enthalpy precision, and mass of both the housing pan and sample. Given that the machine used is very precise, the uncertainty of c_p is determined here as 0.25 %.

3 Thermal Conductivity: In-Plane

3.1 Thermal Conductivity Measurement: In-Plane

All of the samples' in-plane thermal conductivity is measured using the TET technique. Our laboratory first invented it in 2007 [19]. The TET technique does not need calibration, and it has been shown to be very successful for measuring the thermal diffusivity of fiber- or film-like materials in the in-plane direction with sound accuracy (uncertainty better than 5 %) [25–31]. A schematic of the TET technique is shown in the inset of Fig. 3a. The approach calculates the thermal diffusivity by detecting the transient temperature change across the sample where a step voltage rise is induced by Joule heating using a step DC current. It is plausible to assume that the heat conduction is one-dimensional because of the sample's large length-to-thickness ratio. The initial condition for this problem is $T(x)=T_0$ (T_0: ambient temperature). Since the sample is suspended on two bulk aluminum (Al) electrodes, which act as a thermal reservoir, this would result in $T(x=0, t)=T(x=L, t)=T_0$. A linear R-T correlation is applicable within a moderate temperature rise (ΔT typically <4 K) of each measurement. The normalized voltage rise $V^*(t) = [V(t) - V_0]/(V_1 - V_0)$ is equal to the normalized temperature rise $T^*(t) = [T(t) - T_0]/(T_1 - T_0)$, where V_0 is the initial voltage, T_1 and V_1 are the voltage and temperature at the final steady state, respectively. Details of the temperature evolution in TET can be found in our previous works [19, 25], where the normalized temperature rise expression is calculated and used for data fitting and determining the thermal diffusivity. The solution can be spelled out as below

$$T^* = \frac{96}{\pi^4} \sum_{m=1}^{\infty} \frac{1 - \exp[-(2m-1)^2\pi^2\alpha_{\mathrm{eff}}t/L^2]}{(2m-1)^4}, \tag{2}$$

where α_{eff} is the thermal diffusivity containing the radiation effect, and L is the sample's length.

As illustrated in Fig. 3a, the experiment begins with the sample being connected to two Al electrodes using a silver paste to provide reliable thermal and electrical connections. One of the uncoated macro-porous layer samples under study, measuring 1320 µm in length and 655 µm in width, is shown in Fig. 3b. Additionally, a sample of the double-layer GDL studied here, measuring 1590 µm in length and 695 µm in width, is shown in Fig. 3c.

As will be discussed in the next section, in order to rule out the radiation effect on α_{eff}, samples of different lengths were measured. Figure 3(d) shows the fitting results of the raw TET data measured for three samples of the uncoated macro-porous layer with lengths of 3752 µm, 2986 µm, and 2297 µm. These samples' thermal diffusivity (α_{eff}) is determined as $5.3 \times 10^{-6} \pm 1.72 \times 10^{-8}$, $4.6 \times 10^{-6} \pm 3.24 \times 10^{-8}$, and $4.56 \times 10^{-6} \pm 2.16 \times 10^{-8}\ \mathrm{m^2 \cdot s^{-1}}$ in the in-plane direction, respectively. On the other hand, Fig. 3(e) shows three samples of the double-layer GDL with lengths of 5172, 4416, and 2400 µm, carrying α_{eff} values of $3.39 \times 10^{-6} \pm 4.95 \times 10^{-9}$, $3.97 \times 10^{-6} \pm 1.39 \times 10^{-8}$, and $2.80 \times 10^{-6} \pm 1.15 \times 10^{-8}\ \mathrm{m^2 \cdot s^{-1}}$, in the in-plane direction, respectively. It is evident that a sound fitting can be obtained with a

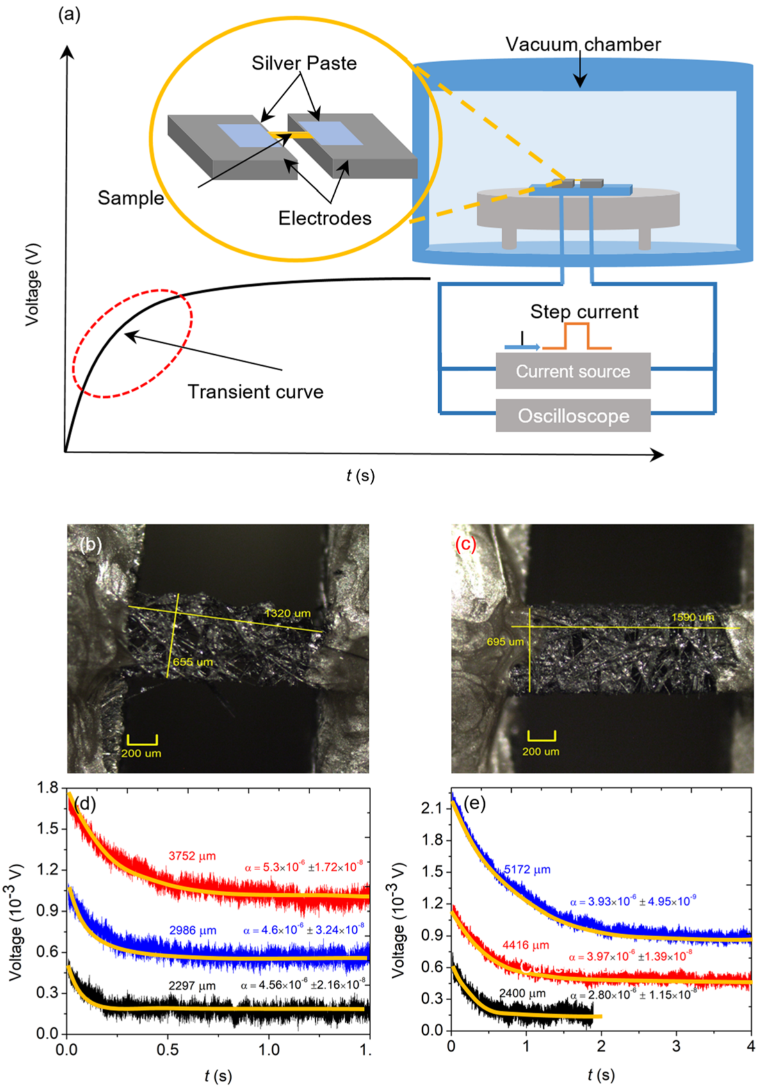

Fig. 3 (a) Schematic illustrating the vacuum chamber, the step current used in the TET measurement, and the experimental concept alongside the methodology for determining thermal diffusivity based on the transient curve of the experimental *V*-*t* signal. (b) A suspended uncoated macro-porous layer sample used for TET measurement. (c) A suspended double-layer GDL sample used for TET measurement. (d) The fitting results of an uncoated macro-porous layer sample's raw TET signals (experimental data). (e) The fitting results of the raw TET signals (experimental data) of a double-layer GDL sample

relative uncertainty in the range of < 0.70 %. Figure 3d and e also show that longer samples have larger effective thermal diffusivities. This is due to the radiation effect and will be analyzed in the next section. Please note that the sample is housed in a vacuum chamber of 7 μbar pressure for TET measurements to make the convection effect negligible.

3.2 Effect of Radiation

After α_{eff} is determined, the intrinsic thermal diffusivity α value in the in-plane direction is determined by taking out the radiation contribution, which has been detailed previously in References [25, 27, 30]. Considering the radiation effect, we have,

$$\alpha_{\mathrm{eff}} = \alpha + \frac{8\varepsilon\sigma T^3 L^2}{\pi^2 D\rho c_{\mathrm{p}}}, \tag{3}$$

where ε is the surface emissivity, σ the Stefan–Boltzmann constant, D sample's thickness, ρ is the density, and T the sample's temperature. It is perceivable from Eq. 3 that α_{eff} has a linear relationship with the sample's squared length, given that the slope is $8\varepsilon\sigma T^3/(\pi^2 D\rho c_{\mathrm{p}})$. Multiple samples of different lengths are measured to subtract the radiation effect. Figure 4 shows the results for the uncoated macro-porous layer and double-layer GDL measurements. As can be seen, a linear relationship is observed between α_{eff} and L^2. The y-axis intercept in Fig. 4 is the value of α without radiation effect: α which is found to be $3.05 \times 10^{-6}\ \mathrm{m}^2 \cdot \mathrm{s}^{-1}$ with an uncertainty of 3.8 % for the uncoated macro-porous layer, and $2.65 \times 10^{-6}\ \mathrm{m}^2 \cdot \mathrm{s}^{-1}$ with an uncertainty of 4.0 % for the double-layer GDL. Using the relation between thermal diffusivity and thermal conductivity [32] where $k = \alpha \cdot \rho c_{\mathrm{p}}$, the thermal conductivities (k) in the in-plane direction of the uncoated macro-porous layer is determined to be $1.05\ \mathrm{W} \cdot \mathrm{m}^{-1} \cdot \mathrm{K}^{-1}$ with an uncertainty of 4.5 %, and $1.53\ \mathrm{W} \cdot \mathrm{m}^{-1} \cdot \mathrm{K}^{-1}$ with an uncertainty of 4.7 % for the double-layer GDL. The double-layer GDL has an in-plane thermal conductivity that is improved by 50 % over the macro-porous layer, which is uncoated and unsupported by the MPL.

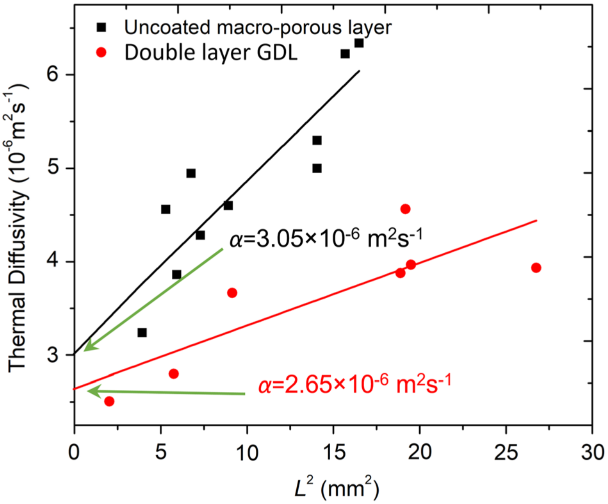

Fig. 4 Effective thermal diffusivity of the uncoated macro-porous layer and the double-layer GDL samples of different lengths in the in-plane direction against the squared length, highlighting the y-intercept

4 Thermal Conductivity: Out-of-Plane

The differential thermal resistance (DTR) technique is used in this work to measure the out-of-plane thermal conductivity. This method was invented by our lab and has been validated by measuring reference samples like PMMA and glass, with a small measurement uncertainty (better than 5 %) [20]. Figure 5a shows a schematic of the DTR technique. The top and bottom surfaces of the sample are covered by one-layer double-sided adhesive black tape, and they are secured to an Al substrate. The black tape guarantees maximized laser absorption and sound contact with the sample and substrate. Based on the thermal resistance circuits of the sample case provided in Fig. 5b, the temperature rise of the sample is dependent on Q, R_{rc}, R_t, R_s, and R_{sub}. More details of these parameters are provided in the caption of Fig. 5. In order to obtain several unknown parameters in the sample case, including the thermal resistance of radiation-convection, tapes, and substrate, two other cases (fused glass and two-layer black tapes) have been added to the experiment. Notably, fused glass thermal conductivity (i.e., thermal resistance) is known as $1.4\ \mathrm{W \cdot m^{-1} \cdot K^{-1}}$ [24]. More details of DTR physical principles can be found in our previous work [20]. Detecting the temperature rise of three cases by the infrared camera while they are exposed

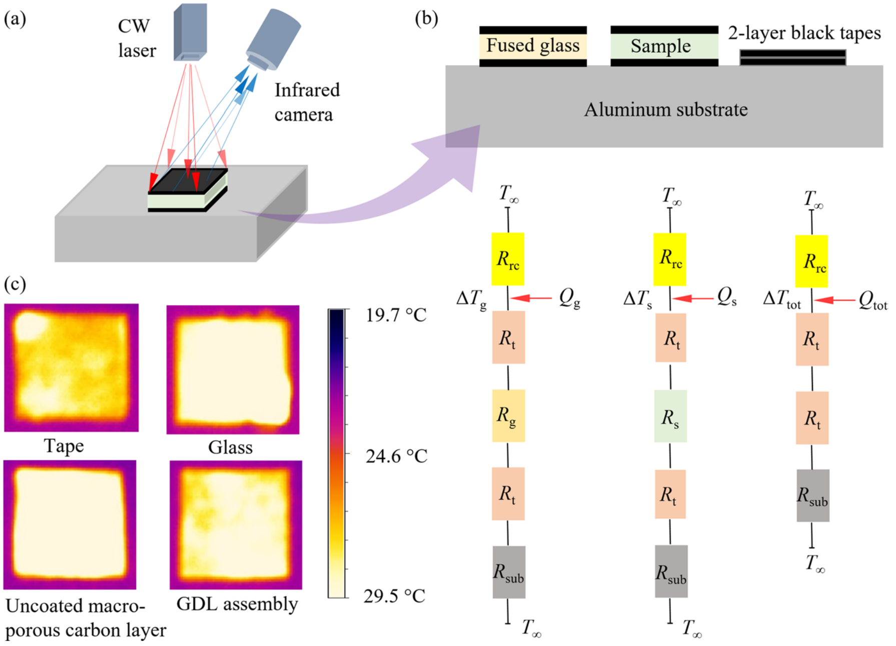

Fig. 5 (a) Schematic of the DTR technique for measuring the out-of-plane thermal conductivity of the sample. (b) Three cases used in the experiment with their corresponding thermal circuits. The symbols represent the following: Q for absorbed laser power, R_{rc} for radiation-convection, R_t for black tape, R_s for sample, R_g for glass, R_{sub} for Al substrate thermal resistances, and ΔT for a temperature rise of each case measured by the infrared camera. (c) Uniform temperature rise of sample surface for different cases

to the 1550 nm laser beam leads to obtaining the thermal resistance of the sample using Eqs. 4–6 listed below:

$$Q_{\mathrm{tot}} = \Delta T_{\mathrm{tot}} \left[\frac{1}{(R''_{\mathrm{rc}}/A_{\mathrm{tape}})} + \frac{1}{(R''_{\mathrm{tot}}/A_{\mathrm{tape}})} \right], \tag{4}$$

$$Q_{\mathrm{s}} = \Delta T_{\mathrm{s}} \left[\frac{1}{(R''_{\mathrm{rc}}/A_{\mathrm{s}})} + \frac{1}{(R''_{\mathrm{tot}}/A_{\mathrm{s}}) + (R''_{\mathrm{s}}/A_{\mathrm{s}})} \right], \tag{5}$$

$$Q_{\mathrm{g}} = \Delta T_{\mathrm{g}} \left[\frac{1}{(R''_{\mathrm{rc}}/A_{\mathrm{g}})} + \frac{1}{(R''_{\mathrm{tot}}/A_{\mathrm{g}}) + (R''_{\mathrm{g}}/A_{\mathrm{g}})} \right], \tag{6}$$

where Q, ΔT, and A refer to the absorbed laser power, surface temperature rise, and surface area, respectively. In addition, the subscripts represent the following: "tot" for the combination of two black tapes and the Al substrate, "rc" for radiation and convection, "s" for sample, and "g" for glass. In the equations mentioned above, R'' is the unit area thermal resistance, which is defined as $R'' = R \cdot A = D/k$ for fused glass and sample cases. Note that D is thickness and k is thermal conductivity. Furthermore, R_{tot} and R_{rc} are division of R''_{tot} and R''_{rc} by the area of three different cases in Eqs. 4–6. Theoretically, the relation of R and $1/A$ is not linear for R_{tot} and R_{rc}. The dimensions of the cases have been measured by digital micrometer with an accuracy of 0.001 mm. Although there is a slight difference between the areas of cases, they are very close to each other. Therefore, the linear relation as $R = R''/A$ for R_{tot} and R_{rc} can still be applied. Solving Eqs. 4–6 simultaneously results in R''_{s}, which can be used to calculate the sample's thermal conductivity as $k_{\mathrm{s}} = D/R''_{\mathrm{s}}$.

The above-mentioned experiment is also done under vacuum with a pressure of ~ 20 μbar to ensure negligible convection heat transfer and to decrease the impact of air within the sample's pores. This vacuum condition thermal conductivity measurement will provide valuable information for us to understand the pore/structure's effect on the thermal conductivity. The same procedure is followed after placing three cases inside the vacuum. The ZnSe window embedded in the vacuum chamber allows the laser beam to enter the chamber and the infrared camera to measure the temperature rise. Although the ZnSe window's transparency for the 1550 nm wavelength laser beam is between 60 % and 80 % depending on its thickness and temperature [33, 34], the transmission is directly evaluated by measuring the transmitted laser power inside the vacuum. Furthermore, the ZnSe window's transparency has minimal impact on temperature rise measurement. Table 1 shows details of the experiment in air and vacuum for the uncoated macro-porous layer and the double-layer GDL samples. T_1 and T_2 stand for the temperatures of each case before and after laser irradiation and ΔT indicates the temperature rise. The out-of-plane thermal conductivity for uncoated macro-porous layer sample in air and vacuum is measured to be 0.075 $\mathrm{W \cdot m^{-1} \cdot K^{-1}}$ and 0.051 $\mathrm{W \cdot m^{-1} \cdot K^{-1}}$. Also, for the double-layer GDL sample in air and vacuum, the thermal conductivity is measured as 0.255 $\mathrm{W \cdot m^{-1} \cdot K^{-1}}$ and 0.145 $\mathrm{W \cdot m^{-1} \cdot K^{-1}}$, respectively. The thermal conductivity

Table 1 Experimental results of out-of-plane thermal conductivity measurement in air and vacuum

Experiment data	Fused glass	Tape (2 layers)	Uncoated macro-porous layer	Double-layer GDL
Length (mm)	8.08	8.21	8.103	8.103
Width (mm)	8.20	7.87	8.509	8.179
Thickness (mm)	1.59	0.66	0.100	0.200
Air				
T_1 (°C)	23.4	23.2	23.0	23.3
T_2 (°C)	30.2	27.6	29.4	28.1
ΔT (°C)	6.80	4.40	6.40	4.80
Q (mW)	208	235	187	169
Vacuum				
T_1 (°C)	23.3	23.2	23.5	23.4
T_2 (°C)	31.5	28.3	28.5	28.9
ΔT (°C)	8.20	5.10	5.00	5.50
Q (mW)	230	217	119	144

measurement uncertainty is caused by thickness, area, temperature rise, and laser power measurements for all three cases mentioned earlier. Considering the sample case, the uncertainty of thickness is ± 0.5 %, the uncertainty of area is ± 0.22 % for both air and vacuum, the uncertainty of temperature rise is ± 0.09 % for air and ± 0.10 % for vacuum, and the uncertainty of laser power is ± 0.47 % for air and ± 0.45 % for vacuum. The uncertainty of thermal conductivity is calculated to be ± 2.2 % for measurements in air and vacuum.

5 Physics Discussions

As expected, the thermal conductivity values are lower in vacuum than in air. Since air is almost removed from pores in the vacuum, heat can be transferred only by radiation within the pores, which is much less effective than air convection and conduction. As a result, the thermal conductivity in vacuum is lower than in air. The thermal conductivity difference between air and vacuum values for uncoated macro-porous layer and double-layer GDL samples is 0.024 and 0.110 $\text{W} \cdot \text{m}^{-1} \cdot \text{K}^{-1}$, respectively. The lower bound of this difference is for the parallel configuration between the sample and air inside in the thickness direction as $\Delta k = \varphi \times k_{\text{air}}$, where φ is the sample porosity. Taking graphite density as 2.21 $\text{g} \cdot \text{cm}^{-3}$ [24], the porosity of the uncoated macro-porous layer sample is calculated to be 82 %. Therefore, Δk can be estimated as 0.021 $\text{W} \cdot \text{m}^{-1} \cdot \text{K}^{-1}$, which is very similar to our measurement (0.024 $\text{W} \cdot \text{m}^{-1} \cdot \text{K}^{-1}$). Consequently, the uncoated macro-porous layer and air within the sample follow a quite parallel configuration, but still has some serial configurations in the thickness direction. We are unable to calculate the porosity of the double-layer GDL sample due to the lack of its theoretical full density. However, its thermal conductivity difference between air and vacuum ($0.110\ \mathrm{W \cdot m^{-1} \cdot K^{-1}}$) is much higher than air's thermal conductivity. This firmly concludes that the sample and air within its pores have more serial connections in the thickness direction.

It should be noted that the double-layer GDL consists of a MPL and coated macro-porous layer with PTFE. Theoretically, this relation $(t/k)_{\mathrm{GDL\ assembly}} = (t/k)_{\mathrm{MPL}} + (t/k)_{coated\ carbon\ layer}$ describes the contribution to thermal conductivity by the two layers within the double-layer GDL. In this relation, t is thickness and k is thermal conductivity. The coated carbon layer in this relation represents the macro-porous layer sample coated with PTFE, and its thermal conductivity is unknown to us because our single GDL sample is a macro-porous layer with no PTFE coating. As a result, it is impractical to use the above relation to calculate the MPL's intrinsic thermal conductivity. However, $(t/k)_{coated\ carbon\ layer}$ should be smaller than $(t/k)_{\mathrm{GDL\ assembly}}$. Note that the thickness of the GDL assembly and coated carbon layer is 0.2 and 0.1 mm, respectively. In addition, the thermal conductivity of the GDL assembly is $0.255\ \mathrm{W \cdot m^{-1} \cdot K^{-1}}$ in air and $0.145\ \mathrm{W \cdot m^{-1} \cdot K^{-1}}$ in vacuum. Consequently, using $(t/k)_{coated\ carbon\ layer} < (t/k)_{\mathrm{GDL\ assembly}}$, the thermal conductivity of the coated carbon layer can be roughly estimated to be higher than $0.128\ \mathrm{W \cdot m^{-1} \cdot K^{-1}}$ in air and $0.073\ \mathrm{W \cdot m^{-1} \cdot K^{-1}}$ in vacuum, which is higher than the uncoated macro-porous layer's measured thermal conductivity in this work ($0.075\ \mathrm{W \cdot m^{-1} \cdot K^{-1}}$ and $0.051\ \mathrm{W \cdot m^{-1} \cdot K^{-1}}$ in air and vacuum). This means the PTFE coating increases the macro-porous layer's thermal conductivity. This conclusion agrees with the theory since air with a lower thermal conductivity ($0.026\ \mathrm{W \cdot m^{-1} \cdot K^{-1}}$ [24]) has been replaced by PTFE with a higher thermal conductivity of $0.259\ \mathrm{W \cdot m^{-1} \cdot K^{-1}}$ [35]. Therefore, PTFE has increased the connections between the carbon fibers. However, it contradicts previous studies [12, 36]. There are two possible reasons for this observation. First, decreasing thermal conductivity by adding PTFE to the carbon sheet in previous studies might be related to the orientation of PTFE to the carbon fibers. This might reduce thermal conductivity by blocking direct contact areas between carbon fibers [37]. The second one is that while putting MPL and coated macro-porous layer together in our double-layer GDL sample, the MPL might penetrate into the coated carbon sheet's pores, increasing the contact regions of the macro-porous layer, increasing its thermal conductivity.

Comparing the in- and out-of-plane thermal conductivity of the uncoated macro-porous layer ($1.05\ \mathrm{W \cdot m^{-1} \cdot K^{-1}}$ and $0.051\ \mathrm{W \cdot m^{-1} \cdot K^{-1}}$, respectively) and double-layer GDL ($1.53\ \mathrm{W \cdot m^{-1} \cdot K^{-1}}$ and $0.145\ \mathrm{W \cdot m^{-1} \cdot K^{-1}}$, respectively), it is conclusive that the in-plane thermal conductivity is much higher than out-of-plane one for both samples. As shown in Fig. 2, the macro-porous layer is made of carbon fibers, whose orientation is mostly along the in-plane direction. Therefore, this strong anisotropic structure leads to a much higher in-plane thermal conductivity ($k_{\|}$) than the out-of-plane one ($k_{\perp}$), with a ratio of $k_{\|}/k_{\perp} = 20.6$. However, the MPL layer does not show much structure anisotropy. So, the double-layer GDL anisotropic thermal conductivity is mostly caused by its anisotropic macro-porous layer. Therefore, the anisotropic level is reduced to $k_{\|}/k_{\perp} = 10.6$.

This paper's results are compared with those of references in Table 2. The study in the in-plane direction by Zamel et al. [18] on TORAY-TPGH-120 (0 % PTFE),

Table 2 Comparison of thermal conductivity between the current and previous studies

Direction of study	Materials and remarks	k (W · m^{-1} · K^{-1})		References
In-plane	TORAY carbon paper at -20 to + 120 °C with 0, 5, 30, 50 wt %	10.5–28		[18]
	Uncoated macro-porous layer at room temperature and vacuum (0 % PTFE)	1.05		Current study
	Double-layer GDL at room temperature and vacuum (50 % PTFE + MPL)	1.53		
Out-of-plane	SIGRACET carbon paper 0 wt % PTFE at 56 °C, 2 MPa	0.48 ± 0.09		[12]
	TORAY-TPGH-060 carbon paper at 26 °C, 2 MPa	1.80 ± 0.27		
	SpectraCarb carbon paper at 0.7–13.8 bar, 70 °C	0.26–0.7		[13]
	SolviCore GDL 30 % PTFE + MPL at 0.7–13.8 bar, 70 °C	0.25–0.52		
	TORAY-TPGH-120, 0 wt % PTFE, low compression, temp. -50 to + 120 °C	0.2–0.4		[16]
	Uncoated macro-porous layer at room temperature (0 % PTFE)	Air (~ 1 bar):	0.075	Current study
		Vacuum (~ 20 μbar):	0.051	
	Double-layer GDL at room temperature (50 % PTFE + MPL)	Air (~ 1 bar):	0.255	
		Vacuum (~ 20 μbar):	0.145	

serves as a direct comparison for our macro-porous layer thermal conductivity value in the in-plane direction. Mainly because it is not supported by an MPL and has no PTFE treatment. Zamel et al. [18] measured the in-plane thermal conductivity within a temperature range of − 20 to + 120 °C with various Teflon loadings. They concluded that for 0 % PTFE loading, the thermal conductivity around room temperature is ~ 14 $\text{W} \cdot \text{m}^{-1} \cdot \text{K}^{-1}$. When compared to our uncoated macro-porous layer in-plane thermal conductivity (1.05 $\text{W} \cdot \text{m}^{-1} \cdot \text{K}^{-1}$), a big discrepancy can be noticed. Structural differences, thermocouple uncertainty in their method, as well as the fact that their measurement in the in-plane direction was under atmospheric conditions that is essentially difficult in testing by standard steady-state methods. Our measurement has strictly ruled out the radiation effect, which is critical to measuring low thermal conductivity porous materials.

For the out-of-plane thermal conductivity comparison, we came across the work by Khandelwal and Mench [12]. They reported the out-of-plane thermal conductivity of TORAY-TGP-H-60 carbon paper (78 % porosity, 0 % PTFE) at 26 °C as 1.80 $\text{W} \cdot \text{m}^{-1} \cdot \text{K}^{-1}$, and SIGRACET carbon paper (AA series, 82–85 % porosity, 0 % PTFE) at 56 °C as 0.48 $\text{W} \cdot \text{m}^{-1} \cdot \text{K}^{-1}$, both under 2 MPa, which both can be compared to our uncoated macro-porous layer sample's result. However, their results are higher than our data, which is 0.075 $\text{W} \cdot \text{m}^{-1} \cdot \text{K}^{-1}$ at room temperature in air (~ 0.1 MPa). Note that their first sample's porosity is a little lower than ours, which is 82 %, and it could increase their sample's thermal conductivity. On the other hand, their second sample's porosity is almost the same as ours. However, both the temperature and pressure of their experiment are higher than those in our work. This can explain the difference. The higher temperature will increase the air's thermal conductivity. This will improve the convection and conduction within pores, thereby increasing the overall thermal conductivity. Chen et al. [38] reported that the thermal conductivity of GDL increases ~ 21 % by increasing temperature from 25 °C to 90 °C. Zamel et al. [16] reported the out-of-plane thermal conductivity of TORAY-TGP-H-120 carbon paper (0 and 60 % PTFE) increases with the increased temperature. This is due to the fact that graphited carbon fibers expand as a result of increasing temperature in the out-of-plane direction, resulting in reduced contact resistances between fibers and increased thermal conductivity. On the other hand, carbon fibers contract with increased temperature in the in-plane direction as TORAY-TGP-H-120 carbon paper's in-plane thermal conductivity decreased in Zamel et al.'s study [18] with increased temperature. The directional dependence of carbon's thermal expansion coefficient is consistent with the work of Tsang et al. [39]. They calculated the thermal expansion coefficient of graphite in out-of-plane and in-plane directions over different temperature ranges. However, the out-of-plane thermal conductivity of TORAY-TGP-H-60 carbon paper has decreased from 1.80 $\text{W} \cdot \text{m}^{-1} \cdot \text{K}^{-1}$ at 26 °C to 1.24 $\text{W} \cdot \text{m}^{-1} \cdot \text{K}^{-1}$ at 73 °C in Khandelwal and Mench's work [12]. This inverse trend can be explained due to the presence of carbonized thermo-setting resin [40], which functions as a binder in the sample. Based on phonon transport theory, as the temperature increases, the thermal conductivity of this thermo-setting resin decreases [41, 42]. Without a binder material, the thermal conductivity of sample will show upward trend, but the change is not much [12]. In addition, increasing the compression level increases the thermal conductivity by reducing the porous structure of the sample and contact resistances between fibers. Zamel et al. [16] reported the increased thermal conductivity of TORAY-TGP-H-120 carbon paper by increasing the compression level, regardless of the amount of PTFE content. Rahbar et al. [20] showed that the thermal conductivity of foam increases from 0.064 $\text{W} \cdot \text{m}^{-1} \cdot \text{K}^{-1}$ to 0.174 $\text{W} \cdot \text{m}^{-1} \cdot \text{K}^{-1}$ by increasing the compression level from 0 % to 75 %. Furthermore, their carbon paper samples are different from ours, and the structure difference also causes the thermal conductivity difference. In addition, Karimi et al. [13] reported the out-of-plane thermal conductivity of Spectra-Card carbon paper (78 % porosity, 0 % PTFE) at 70 °C under different compression loads. Their result under 1.3 bar is about 0.31 $\text{W} \cdot \text{m}^{-1} \cdot \text{K}^{-1}$, which is higher than our result in air (~ 1 bar), which is 0.075 $\text{W} \cdot \text{m}^{-1} \cdot \text{K}^{-1}$. Similarly, higher temperature and lower porosity can cause the thermal conductivity to increase. They also measured the thermal conductivity of SolviCore DGL (30 % PTFE + MPL, ~ 83 % porosity) at 70 °C under different compression loads. Their result under 1.3 bar is about to 0.28 $\text{W} \cdot \text{m}^{-1} \cdot \text{K}^{-1}$, which is in a sound agreement with our result for the double-layer GDL sample which is 0.255 $\text{W} \cdot \text{m}^{-1} \cdot \text{K}^{-1}$ under atmospheric pressure. A small discrepancy could be caused by the difference in temperature and the wt % of PTFE treatment. Moreover, Zamel et al. [16] studied the thermal conductivity of TORAY-TPGH-120 carbon paper (78 % porosity, 0 % PTFE) at different temperatures in low compression state. They measured the out-of-plane thermal conductivity at room temperature as about 0.3 $\text{W} \cdot \text{m}^{-1} \cdot \text{K}^{-1}$. There is a huge difference from our result, which is 0.075 $\text{W} \cdot \text{m}^{-1} \cdot \text{K}^{-1}$ in air for uncoated macro-porous layer sample. Their sample structure difference, larger thickness (6 layers of TORAY carbon paper, totally 2.22 mm), and lower porosity might be responsible for this discrepancy.

6 Conclusion

Two techniques were used to measure the k of GDL structures: the TET technique for in-plane k measurement, and the DTR technique for the out-of-plane k measurement. For the first time the k in both directions (in-plane and out-of-plane) was reported for the double-layer GDL (50 % PTFE + MPL) and uncoated single-layer GDL (0 % PTFE). Both GDLs were studied in vacuum and showed a very anisotropic behavior. First, the in-plane k was measured in a vacuum, and the material showed a k of 1.05 $\text{W} \cdot \text{m}^{-1} \cdot \text{K}^{-1}$ with an uncertainty of 4.5 % for the uncoated macro-porous carbon layer, and 1.53 $\text{W} \cdot \text{m}^{-1} \cdot \text{K}^{-1}$ with an uncertainty of 4.7 % for the double-layer GDL. This study is one of the first to report and investigate the k for such double-layer GDL (50 % PTFE + MPL) in the in-plane direction.

The double-layer GDL has an in-plane k that improved by 50 % more than that uncoated and unsupported by the MPL layer. Moreover, the out-of-plane k of both samples was studied in air and vacuum with 2.2 % uncertainty. The k of the uncoated macro-porous layer in air and vacuum was measured as 0.075 $\text{W} \cdot \text{m}^{-1} \cdot \text{K}^{-1}$ and 0.051 $\text{W} \cdot \text{m}^{-1} \cdot \text{K}^{-1}$, and for double-layer GDL the k was measured as 0.255 $\text{W} \cdot \text{m}^{-1} \cdot \text{K}^{-1}$ and 0.145 $\text{W} \cdot \text{m}^{-1} \cdot \text{K}^{-1}$, respectively. Comparing the results in air and vacuum led us to a better understanding of the pores structure inside the samples. The difference in k under air and vacuum revealed that the sample and pores inside it follow more parallel configurations than serial for the uncoated macro-porous layer sample (0 % PTFE), while they follow quite serial configurations for the double-layer GDL sample (50 % PTFE + MPL).

Author Contributions QA and MR did experiment, data processing and analysis. MH and HL did structure characterization and analysis. SX and XW conceived the research idea, supervised the project and conducted data analysis. All authors participated in paper writing.

Funding This work was partially supported by the National Key Research and Development Program (2019YFE0119900 for H. L), US National Science Foundation (CMMI2032464 for X. W.), National Natural Science Foundation of China (No. 52106220 for S. X.), Shenzhen Science and Technology Program (RCBS20210706092255073 for M. H), and Natural Science Foundation of Shandong Province (ZR2020ME183 for H. L.).

Declarations

Competing interests The authors declare no competing interests.

References

1. S. Park, J.-W. Lee, B.N. Popov, Int. J. Hydrog. Energy **37**, 5850 (2012)
2. L. Cindrella, A.M. Kannan, J. Lin, K. Saminathan, Y. Ho, C. Lin, J. Wertz, J. Power. Sources **194**, 146 (2009)
3. K. Jiao, J. Park, X. Li, Appl. Energy **87**, 2770 (2010)
4. R. Omrani, B. Shabani, Int. J. Hydrog. Energy **42**, 28515 (2017)
5. P. Costamagna, S. Srinivasan, J. Power Sources **102**, 253 (2001)
6. M.L. Perry, T.F. Fuller, J. Electrochem. Soc. **149**, S59 (2002)
7. P.C. Okonkwo, C. Otor, Int. J. Energy Res. **45**, 3780 (2021)
8. K.A. Nagy, I.Y. Tóth, G. Ballai, Á.T. Varga, I. Szenti, D. Sebők, J. Kopniczky, B. Hopp, Á. Kukovecz, J. Mol. Liq. **304**, 112698 (2020)
9. D. Gerteisen, T. Heilmann, C. Ziegler, J. Power Sources **177**, 348 (2008)
10. M.S. Wilson, J.A. Valerio, S. Gottesfeld, Electrochim. Acta **40**, 355 (1995)
11. H. Xu, M. Bührer, F. Marone, T.J. Schmidt, F.N. Büchi, J. Eller, J. Electrochem. Soc. **168**, 074505 (2021)
12. M. Khandelwal, M. Mench, J. Power Sources **161**, 1106 (2006)
13. G. Karimi, X. Li, P. Teertstra, Electrochim. Acta **55**, 1619 (2010)
14. J. Ramousse, S. Didierjean, O. Lottin, D. Maillet, Int. J. Therm. Sci. **47**, 1 (2008)
15. O. Burheim, P. Vie, J. Pharoah, S. Kjelstrup, J. Power Sources **195**, 249 (2010)
16. N. Zamel, E. Litovsky, X. Li, J. Kleiman, Int. J. Hydrog. Energy **36**, 12618 (2011)
17. E. Sadeghi, N. Djilali, M. Bahrami, J. Power Sources **195**, 8104 (2010)
18. N. Zamel, E. Litovsky, S. Shakhshir, X. Li, J. Kleiman, Appl. Energy **88**, 3042 (2011)
19. J. Guo, X. Wang, T. Wang, J. Appl. Phys. **101**, 063537 (2007). https://doi.org/10.1063/1.2714679
20. M. Rahbar, M. Han, S. Xu, H. Zobeiri, X. Wang, Int. J. Heat Mass Transf. **202**, 123712 (2023)
21. F. Tuinstra, J.L. Koenig, Chem. Phys. **53**, 1126 (1970)
22. A. Patterson, Phys. Rev. **56**, 978 (1939)
23. G. Sun, X. Li, Y. Qu, X. Wang, H. Yan, Y. Zhang, Mater. Lett. **62**, 703 (2008)
24. F.P. Incropera, D.P. DeWitt, T.L. Bergman, *Fundamentals of Heat and Mass Transfer*, 6th edn. (Wiley, Hoboken, 2007)
25. B. Zhu, R. Wang, S. Harrison, K. Williams, R. Goduguchinta, J. Schneiter, J. Pegna, E. Vaaler, X. Wang, Ceram. Int. **44**, 11218 (2018)
26. H. Lin, S. Xu, X. Wang, N. Mei, Small **9**, 2585 (2013)

27. J. Liu, T. Wang, S. Xu, P. Yuan, X. Xu, X. Wang, Nanoscale **8**, 10298 (2016)
28. B. Zhu, J. Liu, T. Wang, M. Han, S. Valloppilly, S. Xu, X. Wang, ACS Omega **2**, 3931 (2017)
29. N. Hunter, A. Karamati, Y. Xie, H. Lin, X. Wang, ChemPhysChem **23**, e202200417 (2022)
30. Q. Alahmad, M. Rahbar, A. Karamati, J. Bai, X. Wang, J. Power Sources **580**, 233377 (2023). https://doi.org/10.1016/j.jpowsour.2023.233377
31. A. Karamati, N. Hunter, H. Lin, H. Zobeiri, S. Xu, X. Wang, Int. J. Heat Mass Transf. **198**, 123393 (2022)
32. R.B. Bird, W.E. Stewart, E.N. Lightfoot, *Transport Phenomena*, 2nd edn. (Wiley, New York, 2007)
33. G. Rusu, M. Diciu, C. Pirghie, E. Popa, Appl. Surf. Sci. **253**, 9500 (2007)
34. M. Ivashchenko, A. Opanasyuk, I. Buryk, V. Lutsenko, A. Shevchenko, J. Nano- Electron. Phys. **9**, 1011 (2017)
35. D.M. Price, M. Jarratt, Thermochim. Acta **392**, 231 (2002)
36. E. Sadeghi, N. Djilali, M. Bahrami, J. of Power Sources **196**, 246 (2011)
37. A. Pfrang, D. Veyret, G. Tsotridis, *Convection and Conduction Heat Transfer*, A. Ahsan edn. (IntechOpen, London, 2011)
38. L. Chen, Y.-F. Wang, W.-Q. Tao, Therm. Sci. Eng. Prog. **19**, 100616 (2020)
39. D. Tsang, B. Marsden, S. Fok, G. Hall, Carbon **43**, 2902 (2005)
40. M. Mathias, J. Roth, J. Fleming, W. Lehnert, W. Vielstich, *Fuel Cell Technology and Applications*, 1st edn. (Wiley, Chichester, 2003)
41. C. Choy, Y. Wong, G. Yang, T. Kanamoto, J. Polym. Sci. Part B **37**, 3359 (1999)
42. L. Song, J.W. Evans, J. Electrochem. Soc. **146**, 869 (1999)

Authors and Affiliations

Qusai Alahmad[1] · **Mahya Rahbar**[1] · **Meng Han**[2] · **Huan Lin**[3] · **Shen Xu**[4] · **Xinwei Wang**[1]

✉ Shen Xu
shxu16@sues.edu.cn

✉ Xinwei Wang
xwang3@iastate.edu

[1] Department of Mechanical Engineering, Iowa State University, 271 Applied Science Complex II, Ames, IA 50011, USA

[2] Shenzhen Institute of Advanced Electronic Materials, Shenzhen Institute of Advanced Technology, Chinese Academy of Sciences, Shenzhen 518055, People's Republic of China

[3] School of Environmental and Municipal Engineering, Qingdao University of Technology, Qingdao 266033, Shandong, People's Republic of China

[4] School of Mechanical and Automotive Engineering, Shanghai University of Engineering Science, Shanghai 201620, People's Republic of China